

# Mechanical Behavior of Methane Infiltrated Coal: the Roles of Gas Desorption, Stress Level and Loading Rate

Shugang Wang · Derek Elsworth · Jishan Liu

Received: 20 April 2012 / Accepted: 16 October 2012  
© Springer-Verlag Wien 2012

**Abstract** We report laboratory experiments to investigate the role of gas desorption, stress level and loading rate on the mechanical behavior of methane infiltrated coal. Two suites of experiments are carried out. The first suite of experiments is conducted on coal (Lower Kittanning seam, West Virginia) at a confining stress of 2 MPa and methane pore pressures in the fracture of 1 MPa to examine the role of gas desorption. These include three undrained (hydraulically closed) experiments with different pore pressure distributions in the coal, namely, overpressured, normally pressured and underpressured, and one specimen under drained condition. Based on the experimental results, we find quantitative evidence that gas desorption weakens coal through two mechanisms: (1) reducing effective stress controlled by the ratio of gas desorption rate over the drainage rate, and (2) crushing coal due to the internal gas energy release controlled by gas composition, pressure and content. The second suite of experiments is conducted on coal (Upper B seam, Colorado) at confining stresses of 2 and 4 MPa, with pore pressures of 1 and 3 MPa, under underpressured and drained condition with three different loading rates to study the role of stress level and loading rate. We find that the Biot coefficient of coal specimens is  $<1$ . Reducing effective confining stress decreases the elastic modulus and strength of coal. This study has

important implications for the stability of underground coal seams.

**Keywords** Coal · Mechanical behavior · Gas desorption · Energetic failure · Gas outbursts

## 1 Introduction

In general, geomechanical failures in coal mines are referred to as rockfalls, bumps, outbursts, pillar failures and squeezes and pillar runs. Rockfalls are relatively non-violent failures of loose rocks due to gravity, whereas rockbursts are violent failures of rocks under high stress that result in significant damage to excavations. Bumps are usually violent failures or movements of coals that do not necessarily cause significant damage within an excavation. Outbursts usually occur in coals and involve catastrophic ejections of coals and gases caused by the sudden release of adsorbed or entrapped gases resulting from the processes of coal deformation and failure (Beamish and Crosdale 1998; Cook 1976; Lama and Bodziony 1998; Shepherd et al. 1981; Tang et al. 2002; Zhu et al. 2007). Coal and gas outbursts may range from being barely noticeable, to cause significant damage to excavations and equipment and possibly even resulting in fatalities. In the last 150 years, more than 30,000 outbursts have occurred in the world coal mining industry (Lama and Bodziony 1998). The largest recorded outburst in a coal mine ejected 14,500 tonnes of coal with 600,000 m<sup>3</sup> of gas and occurred in the Gagarin Colliery, Donetsk basin in the Ukraine (Beamish and Crosdale 1998; Hargraves 1980; Lama and Bodziony 1998). The most disastrous mine outbursts resulted in 187 deaths in the Piast area of Nowa Ruda Colliery in the Lower Silesian coal basin in 1941 (Lama and Bodziony

---

S. Wang (✉) · D. Elsworth  
Department of Energy and Mineral Engineering, G3 Center  
and Energy Institute, The Pennsylvania State University,  
230 Hosler Building, University Park, PA 16802, USA  
e-mail: shugangwang@gmail.com

J. Liu  
School of Mechanical and Chemical Engineering,  
The University of Western Australia, Crawley, Australia

1998) and in 214 deaths in the Sunjiawan coalmine in Fuxin city, China, in 2005 (Li et al. 2007). Of the 16 countries where outbursts occurred, the depth of the ruptured coal seams ranged from as shallow as 41 m to as deep as 1,000 m, in which gases were CH<sub>4</sub> and/or CO<sub>2</sub> and coal was either bituminous or anthracite (Beamish and Crosdale 1998; Lama and Bodziony 1998; Liu et al. 2008). With extensive research into violent failures in coal mines, some progress has been made in the past 100 years towards understanding principal mechanisms (Shepherd et al. 1981). It is generally accepted that prediction of such events in terms of magnitude and time has not been successful (Szwedzicki 2003). As mines progress into deeper and gassier coalbeds, the prediction and prevention of these low-probability/high-consequence events are of utmost importance for the coal mining industry worldwide (Wang et al. 2012b).

The causes and mechanisms for gas outbursts are complex and have been recently reviewed from the perspectives of field data (Hargraves 1980), geological structures (Shepherd et al. 1981), coal type (Beamish and Crosdale 1998), and control and prevention (Diaz Aguado and Gonzalez Nicieza 2007; Lama and Bodziony 1998; Li and Hua 2006). Although several models and theories have been proposed including “pocket”, “dynamic”, “spherical shell” and “multiple factor” models, each of these theories captures only a few of the important features of the critical processes. None gives the complete picture, and none yields quantitative measures to predict and prevent coal outbursts (Guan et al. 2009; Lama and Bodziony 1998; Shepherd et al. 1981). Many of the arguments lack supporting data and have in many cases been deficient due to the inability to accurately measure in situ stress and gas pressure, to examine coal properties at the various scales, and to map underground geological structures, a priori, which may have been the main reasons for the failure to predict most outbursts (Shepherd et al. 1981). It is extremely difficult to formulate a comprehensive theory for outburst mechanisms based on the current knowledge of coal–gas conditions. So far the following factors are believed to play a dominant role in gas outbursts (Fig. 1): (1) geological structures: particularly steeply dipping seams, faults, dykes, and mylonite; (2) gas in coal related to: (a) composition, (b) pressure, (c) content, (d) sorption capacity, and (e) desorption rate; (3) stress level and stress state at the mining face associated with: (a) development of cracking and crushing of coal; (b) changes in permeability of coal seams and redistribution of gas pressure; (c) transfer of pressure from the static phase into a dynamic phase as a result of destruction of the coal seam; and (4) properties and structures of coal seams: (a) strength, (b) porosity, and (c) permeability (Ates and Barron 1988; Aziz and Ming-Li 1999; Beamish and Crosdale 1998; Cao et al.

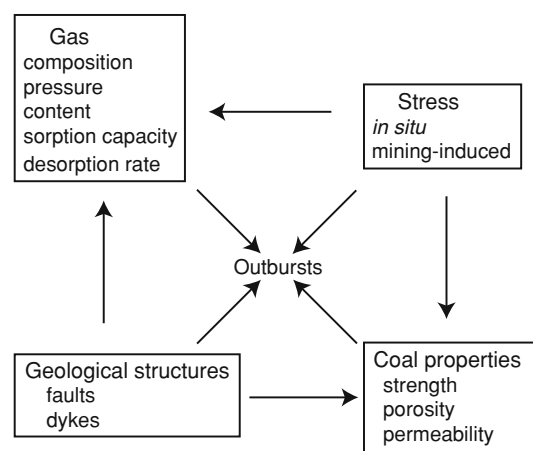


**Fig. 1** A schematic showing the controlling factors to gas outbursts and their interactions

2001; Cyrul 1992; Diaz Aguado and Gonzalez 2009; Durucan and Edwards 1986; Hargraves 1980; Harpalani 1985; Lama and Bodziony 1998; Li 2001; St. George and Barakat 2001; Wold et al. 2008).

In attempting to understand the mechanisms of failure and methods of prevention, a variety of measures have been applied in an attempt to control gas outbursts. In-seam gas drainage (degassing) using surface boreholes, hydraulic fracturing, or directional drilling, and water infusion are probably the most common techniques (Beamish and Crosdale 1998; Lama and Bodziony 1998; Karacan et al. 2011). However, these measures have not completely removed the gas outburst hazard. In summary, although gas outbursts that occur in underground mines have been investigated with vigor, the underlying mechanisms responsible for gas outbursts remain poorly understood. The observational relations are largely anecdotal, and the process-based theories that intend to define mechanisms of outbursts are all lacking in one or more aspects. The low-probability of these events results in long recurrence periods, and severely limits the potential to observe key physical processes in situ, and to therefore discriminate between cause and effect. This lack of understanding seriously limits our ability to forecast gas outbursts.

In this study, we propose that the physical behavior responsible for the energetic failure of coal is entirely consistent with coal viewed as a dual porosity–dual permeability–dual stiffness continuum (Bai and Elsworth 2000; Elsworth and Bai 1992; Wang et al. 2011, 2012a, b) where strength is indexed relative to effective stresses, and where effective stresses are controlled by the pore pressure in the fracture system. The relative roles of stress level and loading rate, deformation and fracture of coal, and their interactions with gas desorption and transport are intimately connected to the rapid dynamic pressurization and

catastrophic failure in underground coal mines. These interplays are inadequately understood, and bear significantly on understanding failure modes, timing, and in defining adequate precursory signatures that may signal the onset of failure. Here, we report systematic experiments that investigate the role of gas desorption, stress level and loading rate on the failure behavior of coal. Two suites of experiments are performed in this study. The objective of the first suite of experiments is to examine the role of gas desorption on failure behavior. We control the initial gas pressures in the fracture and manipulate the gas pressure in the matrix to drive either gas sorption or gas desorption process during deviatoric loading until macroscopic failure. We then examine the difference in failure behavior to explore the role of gas desorption. We use bituminous coal from the Lower Kittanning seam, West Virginia for the first suite of experiments. The objective of the second suite of experiments is to investigate the roles of stress level and loading rate on failure behavior. We investigate the failure behavior of coal with the same pore pressure distribution in the specimens while varying confining stress and loading rate. These experiments are conducted on bituminous coal from the Upper B seam, Colorado.

## 2 Experimental Method

In this section, we will describe the experimental apparatus used in this study, the experiment procedure, and the properties of the coal specimens.

### 2.1 Experimental Apparatus

The experimental apparatus used in these experiments is shown schematically in Fig. 2. This experimental apparatus consists of a Temco triaxial core holder with throughflow and confinement applied by three ISCO pumps. Upstream and downstream gas reservoirs allow pulse testing for permeability, and axial deformation is measured by a linear variable displacement transducer (LVDT). Gas supply is by three gas tanks and three air regulators (for He, CO<sub>2</sub>, CH<sub>4</sub>). Ancillary components are a vacuum pump, two pressure transducers, an acoustic emission system, a gas chromatography, and ten valves. The triaxial core holder is capable of accepting membrane-sheathed cylindrical specimens (2.5 cm diameter and 5 cm long) and of applying independent loading in the axial and radial directions. Confining and axial stresses are applied by a dual cylinder syringe pumps with control resolved to  $\pm 1$  kPa. The cylindrical specimen is sandwiched within the Temco core holder between two cylindrical stainless steel loading platens with through-going flow connections and flow distributors. The specimen and axial platens are isolated from the confining

fluid by a PVC rubber jacket. The end-platens are connected to two low-volume stainless steel gas reservoirs through tubing and isolating valves with the pressure pulse decay method applied to measure permeability. The volumes of these interchangeable upstream and downstream reservoirs are 17.36 and 3.1 cm<sup>3</sup>, respectively. Upstream and downstream fluid pressures are measured by pressure transducers to a resolution of  $\pm 0.03$  MPa. The gas-pressurized upstream reservoir is discharged through the specimen to the downstream reservoir with equilibration time defining permeability of the specimen (Brace et al. 1968; Hsieh et al. 1981). Temperature control jackets are used for all hydraulic pumps and gas reservoirs to maintain fluid temperature to within  $\pm 0.1$  °C. Axial displacement is measured externally using a LVDT in contact with the moving piston to a resolution of  $\pm 1$   $\mu\text{m}$ . Radial displacement is measured from volume change in the confining fluid also to  $\pm 1$   $\mu\text{m}$ . The stiffness of the loading system is 85 kN mm<sup>-1</sup> and the axial displacement of the specimen is obtained by subtracting the displacement of the loading system from the apparent displacement measured by the LVDT. Axial strain is then calculated with reference to the initial length of the specimen. Pressure, flow rate, and changes in fluid volume of the confining fluid are recovered from the ISCO pump p1 and recorded via (National Instruments) Labview. The output signal from the single LVDT is converted at 16-bit resolution using a 16-channel data acquisition system. All signals are logged digitally at a sampling rate from 1 Hz to 1 kHz.

### 2.2 Experimental Procedure

It is worth noting that the measured pore pressure in this study is the pore pressure in the fracture due to the dual porosity–dual permeability nature of coal. Thus, in the following, measured pore pressures refer to the fluid pressure in the fracture system if no reference to the contrary is made. The first suite of experiments (T3558, T3559, T3560 and T3562) is performed on bituminous coal from the Lower Kittanning seam (West Virginia) recovered as a large block from a depth of 186 m with CH<sub>4</sub> as the permeant. Table 3 summarizes the experimental details for the first suite of tests. Figure 3 shows a photo of specimens and fractures. Figure 4 shows the pore pressure distributions under underpressured, normally pressured and overpressured conditions. The pore pressure measured is the pressure in the fracture and the pressure in the matrix is not measured.

For each test, taking T3556 as an example (Fig. 5a), the pressure pulse decay technique is firstly run to saturate the specimen and to determine the initial permeability (Fig. 5b). We conclude the pressure pulse decay period once the pore pressures in the upstream reservoir and

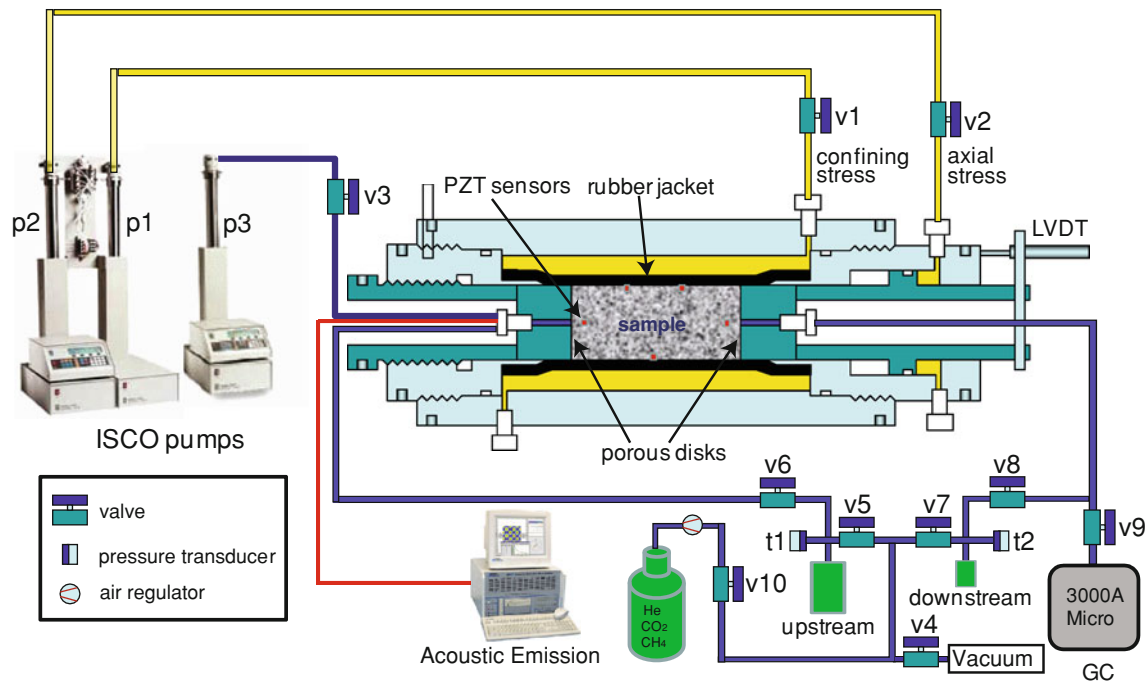


**Fig. 2** Schematic diagram of the experimental apparatus. ISCO pumps apply pressures for confining ( $p1$ ) and axial loads ( $p2$ ). The pressure pulse decay method is used to measure the permeability of coal using upstream and downstream reservoirs. After pressure has

equilibrated in the specimen after a saturation period, the valve  $v6$  is closed and then specimens are loaded to failure with the axial strain and pore pressure being measured by a LVDT and a pressure transducer  $t2$



**Fig. 3** A photo showing specimens and fractures

downstream reservoir are substantially equal (time = 500 s in Fig. 5b). After this, we continue saturating the specimen (durations listed in Table 3) to obtain a desired sorption state (time = 1,100 s in Fig. 5a). Then, we isolate the upstream reservoir from the system (valve  $v6$ ), and manipulate the gas pressure in the matrix to drive either gas sorption or gas desorption process during deviatoric loading until macroscopic failure. To make the pressure in the matrix equal to the pressure in the fracture (normally pressured case), we saturate the specimen for 6 days. To

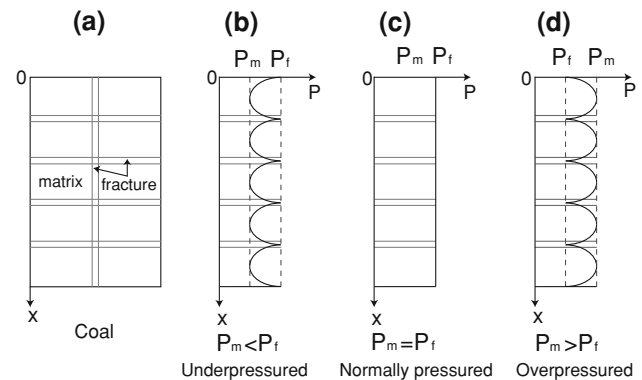


**Fig. 4** Schematic showing pressure distributions in a dual porosity-dual permeability-dual stiffness coal system. **a** A simple fracture-matrix system, **b** underpressured condition when the pore pressure in the matrix is smaller than that in the fracture, **c** normally pressured condition when the pore pressures in the matrix and in the fracture are equal, and **d** overpressured condition when the pore pressure in the matrix is greater than that in the fracture

make the pressure in the matrix larger than the pressure in the fracture (overpressured case), we saturate the specimen for 6 days, and then we reduce the pressure in the gas reservoir. Since the permeability of the fracture is much larger than that in the matrix, the pressure in the fracture dissipates much more quickly. Thus, the pressure in the matrix is larger during the loading process. To make the pressure in the matrix smaller than that in the fracture

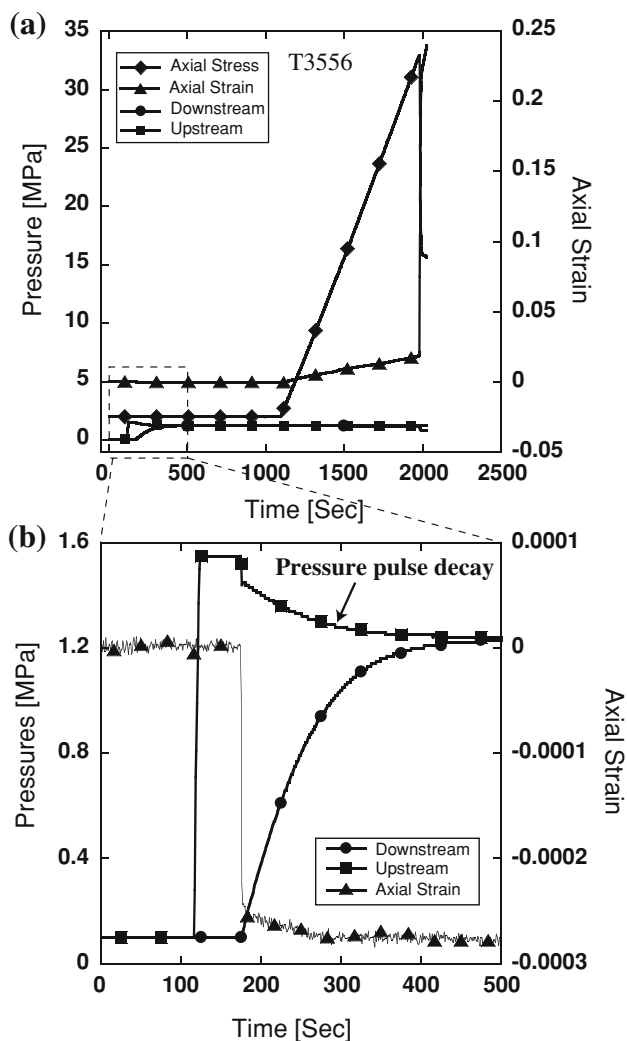


**Fig. 5** Complete permeability measurement and stress–strain history for representative experiment T3556. **a** The entire history of the test including the pressure pulse decay period, the saturation period, and the loading period. Data include upstream pressure, downstream pressure, axial stress, and axial strain. **b** The pressure pulse decay and the axial strain recorded during the decay period. The specimen dilates during the progress of pressure pulse decay period with an axial strain of  $2.8 \times 10^{-4}$ . The specimen fails at 32.9 MPa with a sudden increase in the axial strain at failure

(underpressured case), we saturate the specimen for only 1 h. Since the specimen is not fully saturated in 1 h, the pressure in the matrix is smaller. Closing valve v6 isolates the upstream gas reservoir from the specimen. Then, the external gas reservoir volume consists of the downstream reservoir and a piece of tubing from the specimen to the valve v6. Finally, we apply deviatoric loading to fail the specimen (time from 1,100 to 2,000 s in Fig. 5a). To summarize, Fig. 5a shows the entire history of the test including the pressure pulse decay period, saturation period, and loading period. Data include upstream pressure, downstream pressure, axial stress, and axial strain. Figure 5b only shows the pressure pulse decay and the axial

strain recorded during the decay period. Specifically, we saturate specimen T3558 for 144 h (6 days) after measuring permeability by pressure pulse decay to ensure that the pore pressures in the matrix and in the fracture are equal (1.03 MPa). We define this as a normal pressured specimen. Specimen T3559 is saturated for 1 h after the pressure pulse decay measurement, so that the pore pressure in the matrix is smaller than that in the fracture (pore pressure of 1.01 MPa in the fracture). The matrix is underpressured in this specimen relative to the fracture. Finally, we saturate specimen T3560 for 144 h after the pressure pulse measurement to have equal pore pressures (1.5 MPa) in the matrix and in the fracture, and then we manually reduce the pore pressure in the fracture to 1 MPa instantaneously; so, the pressure in the matrix is larger than that in the fracture. The matrix is overpressured in this specimen relative to the fracture. We then apply deviatoric load at a rate of  $\sim 2.7 \times 10^{-5} \text{ s}^{-1}$  to load these specimens to failure. We monitor pore pressure changes in the downstream reservoir continuously together with volumetric strain to examine specimen compaction and dilation during loading. Axial strain is measured using a LVDT. Lateral strain is measured by measuring the change in the confining fluid. Therefore, volumetric strain is calculated from axial strain and lateral strain. It is worth noting again that the upstream and downstream reservoirs remain of constant volume. Thus, any fluid flowing either in-to or out-from the specimens will change the pressures in these reservoirs. Therefore, trends of pressure change in the reservoirs correspond to changes in void volume of the specimens during the compaction stage prior to the development of micro-cracking. If new fractures are generated, gas in the matrix in the vicinity of the fracture will start to desorb to the new fractures due to the regional pressure differential between the new fractures and the matrix. In this study, we load these three specimens under undrained conditions (hydraulically closed) with a defined (non-zero) volume reservoir. Conversely, specimen T3562 failed under drained conditions (hydraulically open) using the ISCO pump p3 to apply constant pore pressure at 1 MPa throughout the loading but also with a constant volume ( $3.96 \text{ cm}^3$ ) downstream external reservoir.

The second suite of experiments is conducted on bituminous coal from the Upper B seam (Colorado) recovered as a large block from a depth of 610 m. Five tests are carried out under 2 MPa confining stress (3  $\text{CH}_4$ , 1 He and 1  $\text{H}_2\text{O}$  as the permeant) and three under 4 MPa confining stress (3  $\text{CH}_4$ ), with three different loading rates for both stress conditions. All the experiments are performed at 1 MPa effective confining stress. We assume a Biot coefficient of 1, although this value might not be accurate. Detailed experimental conditions and key parameters are listed in Table 4. Specimens are recovered from cores that

**Table 1** Properties of the West Virginia bituminous coal

Proximate analysis			
Fixed carbon	Volatile matter	Ash	
53.36 %	30.23 %	16.41 %	
Ultimate analysis			
Carbon	Hydrogen	Nitrogen	Oxygen
87.00 %	5.60 %	1.46 %	5.94 %
Vitrinite reflectance			
1.01			

**Table 2** Properties of the Colorado bituminous coal

Proximate analysis			
Fixed carbon	Volatile matter	Ash	
65.98 %	24.08 %	9.94 %	
Ultimate analysis			
Carbon	Hydrogen	Nitrogen	Oxygen
86.96 %	5.61 %	1.97 %	5.46 %
Vitrinite reflectance			
1.39			

are drilled parallel to the bedding plane. The mean density of the coals under unconfined conditions is calculated from the mass and volume of the cylindrical cores. This procedure yields average matrix densities of 1,178.5 and 1,132.4 kg m<sup>-3</sup> for the coals from West Virginia and Colorado, respectively. Tables 1 and 2 summarize the proximate analysis and physical properties of the West Virginia coal and the Colorado coal, respectively. The gas used in this study is CH<sub>4</sub> at a purity of 99.995 %.

For the apparatus used in this study, the pore pressure changes in the fracture are recorded in the external reservoir (3.96 cm<sup>3</sup>). To define the drainage state of the specimen, we evaluate the nondimensional strain rate  $\dot{\epsilon}_D$ , defined as

$$\dot{\epsilon}_D = \frac{a^2 \dot{\epsilon} \eta}{k K} \quad (1)$$

where  $a$  is the radius of the specimen,  $k$  is the permeability of the specimen,  $\dot{\epsilon}$  is the strain rate,  $\eta$  is the fluid viscosity, and  $K$  is the bulk modulus of the fluid. The first term indexes the reciprocal fluid drainage rate and the second term represents the rate of pore pressure generation due to the deviatoric loading. When  $\dot{\epsilon}_D$  is small ( $\sim 0$ ), drainage dissipates undrained pore fluid pressures as rapidly as they build, and the system remains drained. When  $\dot{\epsilon}_D$  is a finite number (Rudnicki 1984) or 1 (Samuelson et al. 2009), the system is drained. For our study, using a strain rate of  $\sim 2.7 \times 10^{-5} \text{ s}^{-1}$  and with the measured permeabilities, yields  $\dot{\epsilon}_D$  ranging from 0.006 to 0.049, from which drained conditions may be readily assumed for the specimen. The

purpose of this nondimensional strain rate is to make sure that the pressure measured in the external reservoir is equal to the pressure in the specimen (in the fracture). Since this nondimensional strain rate is small, the pressure buildup due to the loading dissipates rapidly so the system can be considered drained, so the pressure in the external reservoir can be treated as the pressure in the fracture in the specimen.

Figure 5 shows the complete upstream and downstream pore pressures and stress–strain history for a representative experiment T3556 using Helium (He) as the permeant. Since He is inert, specimen T3556 is saturated for only 1,000 s after the equilibrium of the pressure pulse before deviatoric loading. The effective confining stress is 1 MPa for all four tests. Strains are positive in compaction. Dilation (expansion) in the specimen is observed during the progress of the pulse decay period. The specimen fails at 32.9 MPa and the axial strain suddenly increases from 0.0213 to 0.22 at failure, while the pore pressure drops from 1.02 to 0.46 MPa.

### 3 Experimental Observations

In this section, we show the detailed experimental results and analyze the role of gas desorption, stress level and loading rate on the failure behavior of coal. It is worth noting that the role of fractures is hypothesized in this study.

#### 3.1 The Role of Gas Desorption

Figure 6a shows the evolution of deviatoric stress versus axial strain during deviatoric loading for the first suite of experiments. Drained tests at 1 MPa effective confining stress have shown that the coal is an elastoplastic material. Three features are generally evident on the stress–strain curve (Hobbs 1964; Jaeger et al. 2007; Medhurst and Brown 1998). These are: (1) an initial non-linear portion of the stress–strain curve caused by the closing of the preexisting cleats in coal; (2) a range of elastic linearity of stress with strain from which the Young's modulus in compression can be calculated; (3) a final non-linear portion of the stress–strain curve due to pre-rupture cracking. The values of the Young's modulus of the coals tested are given in Table 3. Results show that under the same effective confining stress ( $P_e = \sigma_3 - P_f$ ), the under-pressured specimen has the largest strength and residual strength, followed by the normally pressured specimen, the specimen under drained conditions and then the over-pressured specimen.

Figure 6b shows the evolution of pore pressure with increasing axial strain during deformation. Since experiment T3562 is under a constant pore pressure condition, the pore pressure does not undergo an appreciable change

**Fig. 6** The evolution of **a** deviatoric stress, **b** pore pressure, **c** confining stress, and **d** effective confining stress versus axial strain during deviatoric loading for the first suite of experiments. Results show that under the same effective confining stress, the underpressured specimen has the largest strength and residual strength, followed by the normally pressured specimen, the specimen under drained conditions and then the overpressured specimen. A significant increase in confining stress for the overpressured specimen suggests a relatively dynamic and energetic failure compared with other specimens

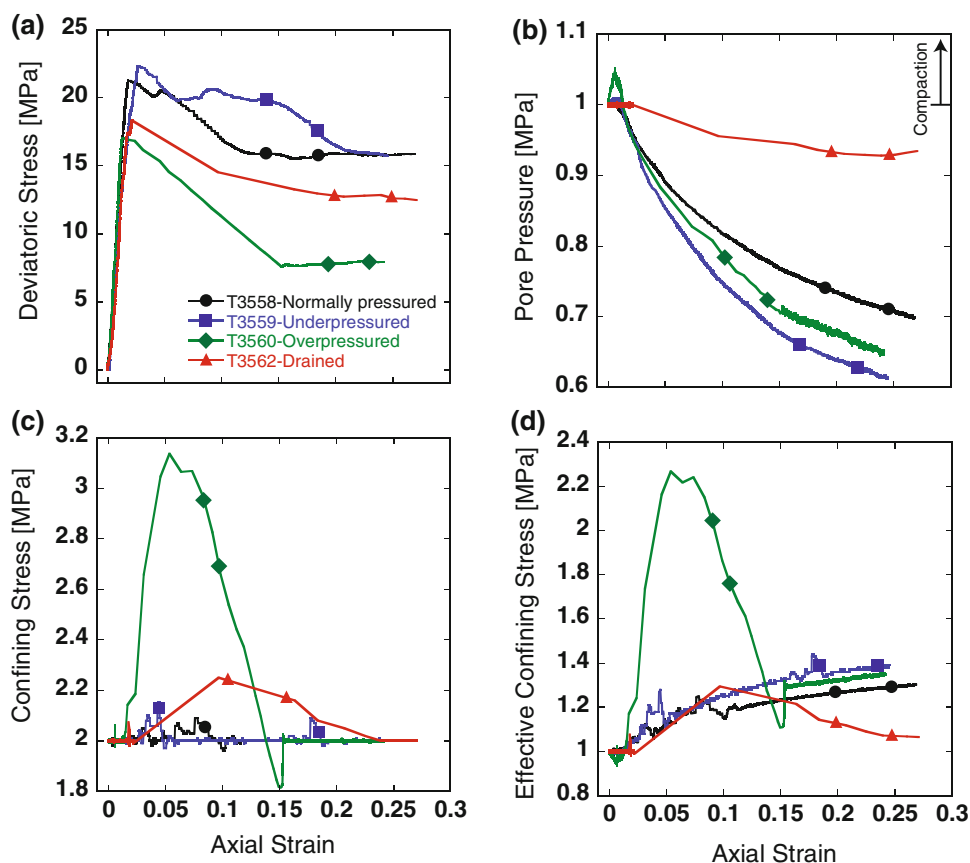


**Table 3** Experimental details for the first suite of experiments

Experiment number	Initial permeability ( $m^2$ )	Saturation time (h)	Confining stress (MPa)	Initial pore pressure (MPa)	Strain rate ( $s^{-1}$ )	Modulus (GPa)	Axial strain at failure (%)	Strength (MPa)	Stress drop (MPa)
T3558	$1.56 \times 10^{-17}$	144	2.03	1.03	$3.3 \times 10^{-5}$	1.36	1.93	24	5.5
T3559	$1.64 \times 10^{-17}$	1	2.00	1.01	$2.7 \times 10^{-5}$	0.92	2.73	24.55	6.35
T3560	$1.28 \times 10^{-17}$	141	2.00	1.00	$2.0 \times 10^{-5}$	1.64	1.40	18.77	9.47
T3562	$4.21 \times 10^{-17}$	42	2.00	1.00	$7.4 \times 10^{-7}$	1.5	2.18	20.63	7.97

during the period of elastic compaction. After the specimen fails, pore pressure gradually drops to 0.94 MPa because the rate of gas pressure dissipation due to the generation of new fracture surface areas outstrips the rate of pressure buildup that the hydraulic pump is able to offer to maintain constant pressure (over the short period of the test). For the overpressured specimen, with increasing strain, pore pressures initially increase due the effects of specimen compaction and methane desorption from the matrix, as anticipated. Pore pressures to decrease once new fractures are generated. Figure 6c shows the resulting changes in confining stress during progressive loading. The confining stresses are applied through the ISCO pump (p1) as shown in Fig. 2. The sudden change in pressure when the sample fails transfers the impact or energy release of the failure to the confining fluid. We observe a significant increase in confining stress

(1.1 MPa) for the overpressured specimen (T3560), which suggests a relatively dynamic and energetic failure compared with other specimens. That is why we observe the dramatic differences in Fig. 6c and d for the overpressured specimen. Subtracting the pore pressures (Fig. 6b) from the confining stresses (Fig. 6c) yields the effective confining stresses (Fig. 6d) that are believed to control the stability of coals, again assuming a Biot coefficient of 1. We observe an increase in confining stresses for all four specimens, with the drained specimen having the smallest increment. The three undrained specimens gained  $\sim 30$ – $40$  % increase in confining stress at  $\sim 20$ – $25$  % axial strain.

To examine whether the effective confining stress is the only factor that controls the failure behavior and strength of coal, we first consider subtracting the induced extra effective stress from the deviatoric stress for every data

point to eliminate the effect, since the maximum induced extra effective stress is only 0.4 MPa. Given that the difference in peak strengths and residual strengths of these four specimens is  $\sim 6$  MPa, subtraction would not make a difference in eliminating the effect. Then, we divide the deviatoric stress by the effective confining stress ( $\sigma_d/\sigma'_c$ ) and also normalize this with its strength value at failure ( $(\sigma_d/\sigma'_c)_D$ ) to check whether the four curves will fall onto the same line (Fig. 7). However, comparing the overpressured specimen with the underpressured specimen, dividing the deviatoric stress by the effective confining stress still shows differences in normalized peak strength ( $\sim 20\%$ ), in post-failure behavior (slope) and in normalized residual strength ( $\sim 48\%$ , Fig. 7a). Dividing and then normalizing still shows differences in post-failure slope and in normalized residual strength ( $\sim 35\%$ , Fig. 7b). Therefore, we speculate that the effective confining stress is not the only factor controlling the strength and failure behavior of coal. We believe that the process of gas desorption from the coal matrix to the fracture is likely to play a significant role in this discrepancy. Next, we evaluate the role of gas desorption in controlling the mechanical response of three undrained specimens (normally pressured, underpressured and overpressured).

Figure 8a shows the deviatoric stress as a function of time for three undrained experiments. All three specimens display a brittle failure behavior with a stress drop. Stress drop is defined as the strength minus the residual strength. We observe that the overpressured specimen experienced the largest stress drop, followed by the normally pressured specimen and then the underpressured specimen. Figure 8b shows the changes in pore pressure during deviatoric loading with time. Three stages can be identified from these curves. These are: the initial compaction stage, cracking stage and macroscopic failure stage. During the initial compaction stage, the pore pressures of the normally pressured and underpressured specimens do not show significant changes. This infers that the  $\sim 1\%$  volumetric strain of the specimens does not significantly influence the pore pressure in the fracture, due to the high compressibility of gas. Similarly, gas sorption from the fracture to the matrix seems to have little effect with the increase in loading and also the time scale of these experiments ( $\sim 400$  s). However, the pore pressure of the overpressured specimen gradually increases with loading, which is likely due to gas desorption from the matrix to the fracture induced by the pore pressure differential. During this micro-fracturing stage, when the specimens begin to dilate, new surface area and crack volume are both generated and thus a decline in pore pressures is expected. Indeed, the underpressured specimen exhibits the largest rate of pore pressure drop, sequentially followed by the normally

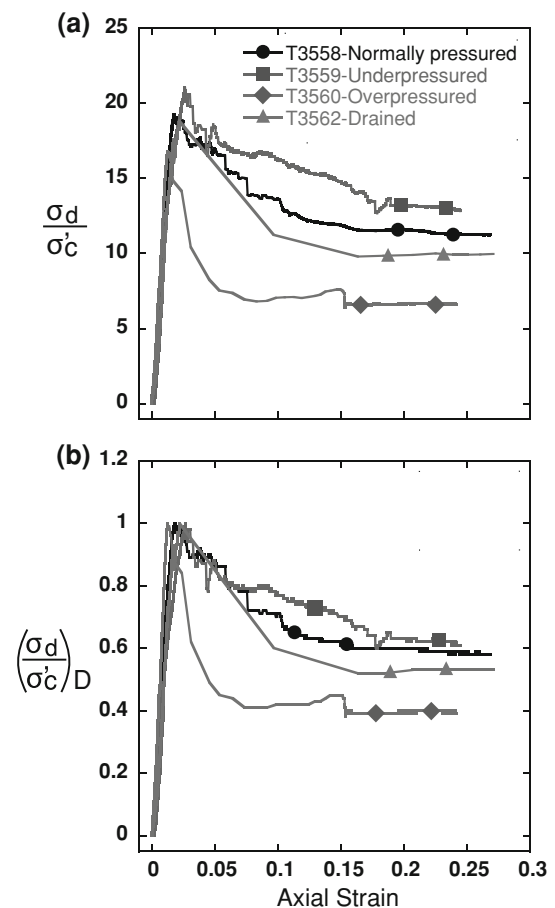


**Fig. 7** **a** Deviatoric stress normalized by the effective confining stress versus axial strain, and **b** the quotient of deviatoric stress and effective confining stress normalized by the strength versus axial strain. The differences in post failure slope and in residual strength in both **(a)** and **(b)** indicate the effective confining stress is not the only factor controlling the strength and failure behavior of coal

pressured specimen and then the overpressured specimen, as expected. Gas desorption from the matrix to the fracture offsets some of the pore pressure decline for the overpressured specimen. That is why its decline rate of gas pressure is the slowest. When the specimens fail, we observe a sudden decrease in pore pressures corresponding to the generation of extensive surface area and volume due to macroscopic failure. As expected, the most rapid and the largest reduction in pore pressure is apparent in the overpressured specimen which is also consistent with the stress drop shown in Fig. 8a and the impact of failure on the confining stress (Fig. 6c). These three features highlight the nature of the energetic failure of the overpressured specimen. The role of rapid gas desorption together with the resulting energy release is apparent in controlling the failure behavior of coal.

Here, we conclude from the first suite of experiments that gas desorption plays a significant role in controlling



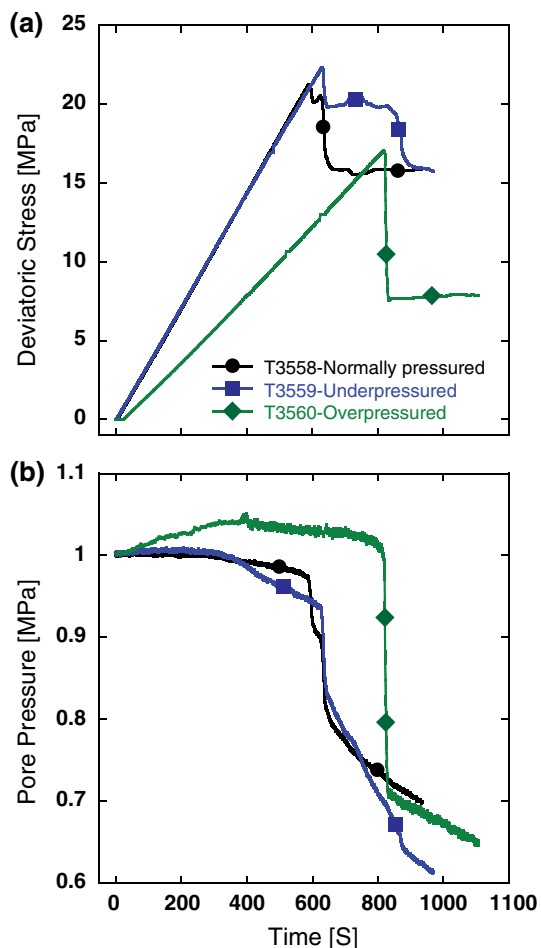


**Fig. 8** **a** Deviatoric stress versus time, **b** pore pressure versus time for the three undrained experiments. The largest deviatoric stress drop and the most rapid and the largest reduction in pore pressure are apparent in the overpressured specimen, which is also consistent with the impact of failure on the confining stress (Fig. 6c). These three features highlight the nature of the energetic failure of the overpressured specimen. The role of rapid gas desorption together with the resulting energy release is apparent in controlling the failure behavior of coal

the mechanical behavior (failure and strength) of coal. In the following, we analyze the effects of confining stress and loading rate on the mechanical response.

### 3.2 The Role of Stress Level and Loading Rate

Eight experiments are conducted to investigate the role of effective confining stress and loading rate with details listed in Table 4. All tests begin with a pressure pulse decay period to measure the initial permeability of the coal specimens. Specimens are then saturated for 24 h before applying deviatoric load with all experiments run at the same effective confining stress (1 MPa) and at room temperature, assuming a Biot coefficient of unity. These include three experiments subject to confining stresses at

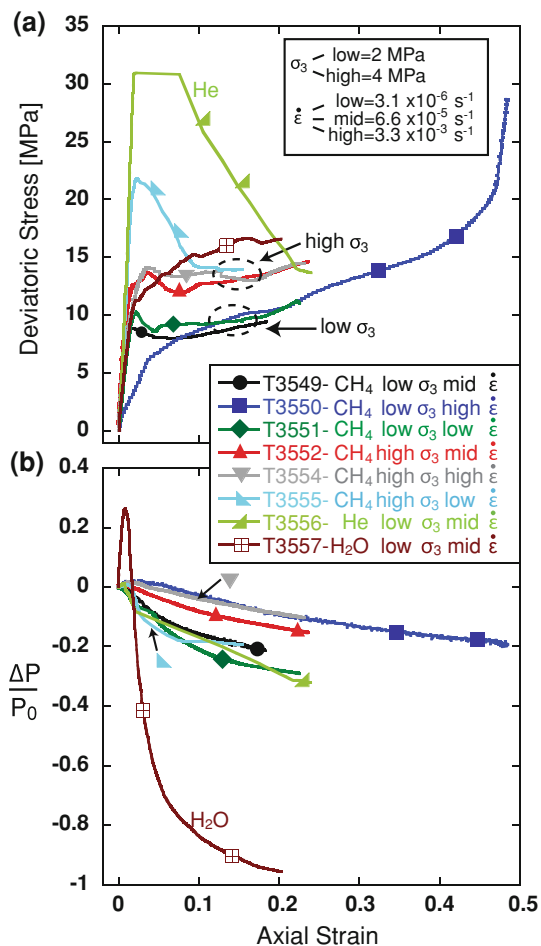
2 MPa and pore pressures at 1 MPa with  $\text{CH}_4$ , three experiments with confining stresses at 4 MPa and pore pressures at 3 MPa with  $\text{CH}_4$ , one experiment at a confining stress of 2 MPa and pore pressure of 1 MPa with He and one experiment with a confining stress of 2 MPa and a pore pressure of 1 MPa with water. Three loading rates are applied for the methane infiltrated specimens ( $3.1 \times 10^{-6} \text{ s}^{-1}$ ,  $6.6 \times 10^{-5} \text{ s}^{-1}$  and  $3.3 \times 10^{-3} \text{ s}^{-1}$ ). With a 24 h saturation period, the pore pressure evolution data after the pressure pulse decay show that the sorption process is not fully completed, so the pore pressure in the matrix is smaller than that in the fracture, which further implies that these specimens are at least slightly underpressured, if not significantly.

Figure 9a shows deviatoric stress versus axial strain during loading for the second suite of experiments. Several features are observed from the stress–strain relationship. Under the same effective confining stress (1 MPa), we note the differences in strength and in residual strength for these two groups of different confining stresses (4 and 2 MPa). Specimens subject to higher confining stress (4 MPa) exhibit higher strength and higher residual strength, which infers that the Biot coefficient is less than unity. The specimen using He as the permeant shows a significantly larger strength suggesting that the gas composition also plays a role in controlling strength. For the six experiments conducted with  $\text{CH}_4$ , experiment T3555 shows a relatively large stress drop of 7.64 MPa at failure. Test T3550 under a high loading rate shows strain hardening behavior without a stress drop, presumably due to dilatancy-induced increase in effective stress. Other specimens exhibit small stress drops, followed by strain hardening. The loading rate shows a positive correlation with the strain hardening behavior. Specifically, specimens under low strain rates show relatively larger stress drops compared with specimens under high loading rates. The single test carried out with water shows a strain hardening behavior without a stress drop at a mid loading rate, which may be attributed to the large dilatancy-induced increase in effective stress. With the same axial strain, much larger compaction and dilation-induced pore pressure changes are observed when using water as the fluid (Fig. 9b), which can be readily explained by the low compressibility of water compared with gases.

We focus on the region where specimens begin to dilate from compaction for the six experiments conducted with  $\text{CH}_4$ . We find that the maximum compaction-induced augmentation in pore pressure increases with increasing loading rate. With a strain rate of the order of  $10^{-3}$ , specimens T3550 and T3554 fail within tens of seconds. This time scale does not allow any significant gas sorption into the coal matrix, and thus the compaction-induced maximum pore pressure augmentation in the fracture is

**Table 4** Experimental details for the second suite of experiments

Experiment number	Initial permeability (m <sup>2</sup> )	Saturation time (h)	Confining stress (MPa)	Initial pore pressure (Mpa)	Strain rate (s <sup>-1</sup> )	Modulus (GPa)	Axial strain at failure	Strength (MPa)	Stress drop (MPa)	Fluid
T3555	$1.08 \times 10^{-16}$	24	4.03	3.03	$1.7 \times 10^{-6}$	1.36	2.19 %	25.8	7.64	CH <sub>4</sub>
T3552	$4.14 \times 10^{-17}$	24	4.04	3.04	$1.2 \times 10^{-4}$	0.96	3.45 %	18.1	1.73	CH <sub>4</sub>
T3554	$2.93 \times 10^{-17}$	24	4.07	3.07	$2.0 \times 10^{-3}$	0.72	3.50 %	19.3	0.74	CH <sub>4</sub>
T3551	$2.21 \times 10^{-16}$	24	1.95	0.95	$4.5 \times 10^{-6}$	0.58	2.05 %	12.2	1.66	CH <sub>4</sub>
T3549	$1.06 \times 10^{-16}$	24	2.05	1.05	$6.0 \times 10^{-5}$	1.01	1.36 %	11.1	0.90	CH <sub>4</sub>
T3550	$9.37 \times 10^{-16}$	24	2.01	1.01	$4.6 \times 10^{-3}$	0.15	4.34 %	8.3	None	CH <sub>4</sub>
T3556	$1.66 \times 10^{-17}$	0.3	2.00	1.00	$2.2 \times 10^{-5}$	2.1	2.13 %	32.9	16.8	He
T3557	$3.26 \times 10^{-17}$	24	2.00	1.00	$6.1 \times 10^{-5}$	0.61	2.21 %	13.5	None	H <sub>2</sub> O



**Fig. 9** **a** Deviatoric stress versus axial strain, **b** normalized pore pressure change versus axial strain for the second suite of experiments for low to high confining stresses and low to high strain rates. Generally, specimens subject to higher confining stress exhibit higher strength and higher residual strength. The loading rate shows a positive correlation with the strain hardening behavior. The specimen using He as the permeant shows a significantly larger strength suggesting that the gas composition also plays a role in controlling strength

larger. After failure, increasing loading rate can lead to less dilatation at a given strain (Brace et al. 1966), so the pore pressure decline rate is smaller for specimens under high loading rate than for those under low loading rate at the same strain.

Figure 10 shows the evolution of normalized pore pressure change, and of specimen volumetric strain with increasing deviatoric stress for the six CH<sub>4</sub> infiltrated specimens. Positive values of specimen volumetric strain and positive normalized pore pressure change correspond to specimen compaction and porosity reduction, respectively. The onset of dilatancy is defined by the stress level at the transition from specimen compaction to dilatancy, corresponding to the peak of the curve representing the change in pore pressure. With increasing confining stress, the onset of dilatancy is shifted to a higher deviatoric stress (Fig. 10). In the elastic compaction regime, the maximum porosity reduction increases with increasing loading rate (Fig. 10a), showing that sorption is a time-dependent process. At a low loading rate, the compaction-induced pore pressure increment in the fractures can be offset to some degree by gas sorption from the fracture into matrix—thus we observe a lower augmentation in the pore pressure. One phenomenon of interest is the lower specimen volumetric strain for the specimen group at the higher confining stress (4 MPa), compared with that for the specimen group at a lower confining stress (2 MPa). This difference may be attributed to the sorption-induced swelling behavior. Studies have shown that it is relatively easier for gas to be adsorbed at a lower confining stress (Hol et al. 2011, 2012a). With the same saturation period (24 h) before the initiation of deviatoric loading, sorption in the specimens under high confining stresses (T3552, T3554 and T3555) is farther from equilibrium sorption when compared with sorption in specimens under low confining stresses (T3549, T3550 and T3551). Thus, even under axial loading, gas sorption may still occur in the specimens under high

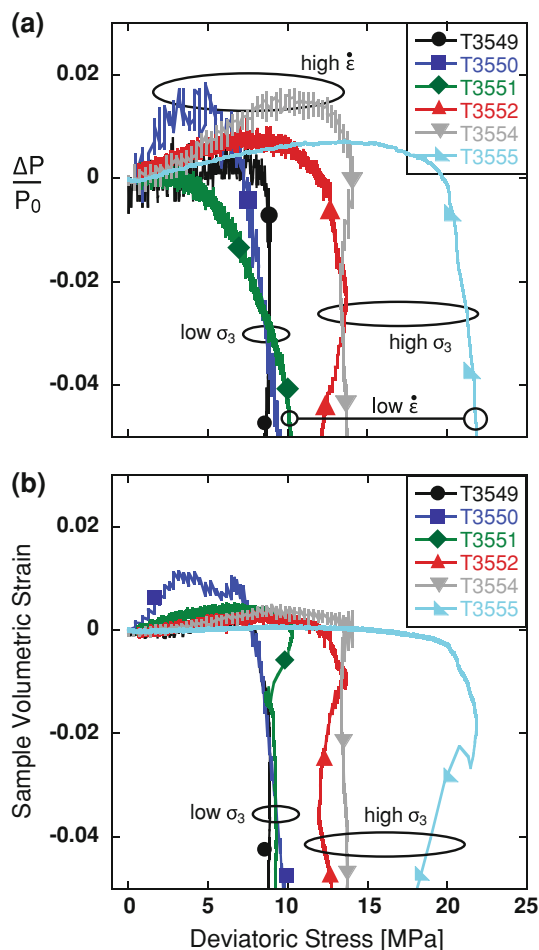


**Fig. 10** **a** Normalized pore pressure change, and **b** specimen volumetric strain versus deviatoric stress for six experiments using  $\text{CH}_4$  as the permeant for low to high confining stresses and low to high strain rates. With increasing confining stress, the onset of dilatancy is shifted to a higher deviatoric stress. In the elastic compaction regime, the maximum porosity reduction increases with increasing loading rate

confining stress. Consequently, the continued swelling of the specimen group at high confining stresses can counteract some of the compaction, which leads to lower net compaction.

Figure 11 shows the effect of confining stress on the Young's modulus and strength of eight experiments. This plot verifies that the Biot coefficient is less than unity for the coal specimens reported here. Under the same confining stress, the He-infiltrated specimen exhibits the largest strength and Young's modulus, implying the weakening effect of gas desorption and the accompanied rapid release of energy due to expansion of the gas. The change in the observed Young's modulus with confining stress is probably due to compaction of the coal matrix and the increasing stiffness of the cleats with stress. Increasing confining stress increases both the modulus and strength for  $\text{CH}_4$  infiltrated specimens, indicating that effective stress is

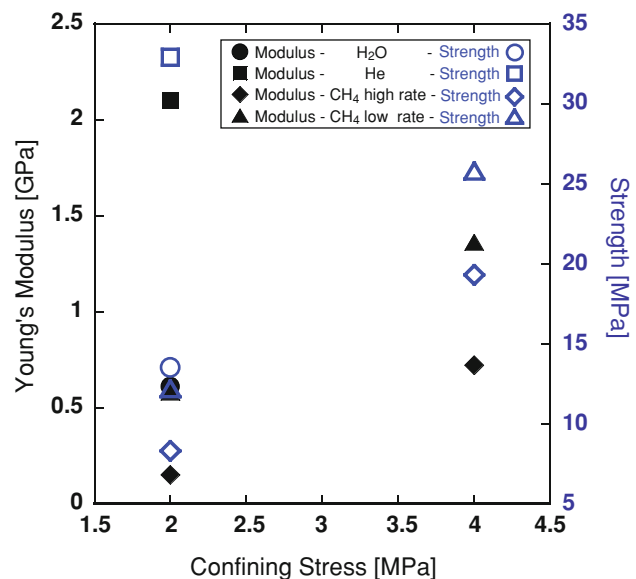


**Fig. 11** Young's modulus and strength versus confining stress for the second suite of experiments with a Biot coefficient less than unity. Increasing confining stress increases both the modulus and strength for  $\text{CH}_4$  infiltrated specimens, indicating that effective stress is one key factor that controls the mechanical response of fractured coal. The Helium infiltrated specimen exhibits the largest strength and Young's modulus, implying the weakening effect of gas desorption and the accompanied rapid release of energy due to expansion of the gas

one key factor that controls the mechanical response of fractured coal.

## 4 Discussions

In this section, we discuss the role of gas desorption, stress level and loading rate on the failure behavior of coal.

### 4.1 The Role of Gas Desorption

It has been long recognized that pore fluid can have a profound influence on the mechanical properties of rocks, and the most important single parameter describing these effects is the pore pressure. This is also true for coal but with significantly more complex phenomena when the pore fluid is a sorbing gas (Wang et al. 2011, 2012a, b; Hol et al. 2012b). Coal is significantly different from other rock types in that it is a naturally fractured dual porosity–dual permeability–dual stiffness sorbing medium (Wang et al. 2011, 2012a, b). In underground coalbeds, more than 90 % of the gas ( $\text{CH}_4$ , or  $\text{CO}_2$ , or mixture) is primarily stored by sorption into the coal matrix (Gray 1987). As much as  $80 \text{ m}^3$  of  $\text{CO}_2$  (Saghafi et al. 2007) and  $40 \text{ m}^3$  of  $\text{CH}_4$  (Faiz et al. 2007) per ton, coal can be adsorbed into the coal matrix, depending on the pressure. This means that a significant quantity of stored energy is accumulated in the coal

matrix and the adsorbed gas has the potential to desorb and release this energy rapidly during micro- or macro-fracturing. Experimental data have shown that mining-induced stresses immediately after excavation can close horizontal cleats (inhibit drainage to the opening) and generate vertical or subvertical cracks (that prompt desorption from the matrix) (Wang et al. 2012b). Since coal is a dual permeability–dual stiffness medium where strength is indexed relative to effective stresses, and where effective stresses are controlled by the pore pressures in the fracture system, this gas desorption increases the pore pressure in the fracture and thus weakens coal according to the principle of effective stress (Fig. 9a). Second, the sudden gas expansion of the desorbed compressible gas phase will release the internal stored energy and in the process will further accelerate the micro-fracturing of the coal. In the field, sudden desorption can be caused by stress unloading after a mining face has advanced. This can also be caused by the mechanical failure of a coal seam due to mining-induced stressing. Once new surfaces are generated, whether these are free faces due to excavation or new fracture surfaces due to cracking, sudden desorption can occur. In the laboratory, this sudden desorption is caused by the generation of new fractures due to the axial loading. Our data are consistent with this view by showing that effective stress effects cannot solely explain the difference in strength and failure behavior between experiments on overpressured and underpressured specimens (Fig. 7). We observe that gas desorption contributes to  $\sim 5$  MPa reduction in the peak and residual strengths in this study. The role of gas desorption is apparent in weakening the coal and in accelerating the rupture process by these dual mechanisms. During the gas desorption process, we speculate desorption rate is the most important parameter to control the energy release rate and the weakening rate/effect. Desorption rate is found to be low for coal with large particle sizes and high for coal with small particle sizes. During cracking, both particle size reduction and gas desorption will have a positive feedback as gas desorption process continue until the coal becomes pulverized, as shown in Fig. 12. This may explain why gas outbursts are rapid, energetic, and catastrophic.

#### 4.2 The Role of Stress Level and Loading Rate

Our data show that Young's modulus and the strength of coal increase with increasing effective confining stress, which is consistent with the literature (Hobbs 1964; Medhurst and Brown 1998). This again confirms the weakening role of gas desorption-induced pore pressure augmentation in the fractures for a drainage-inhibited system. This also implies that the region near the mining face has the largest potential to fail due to the reduction in confining stress

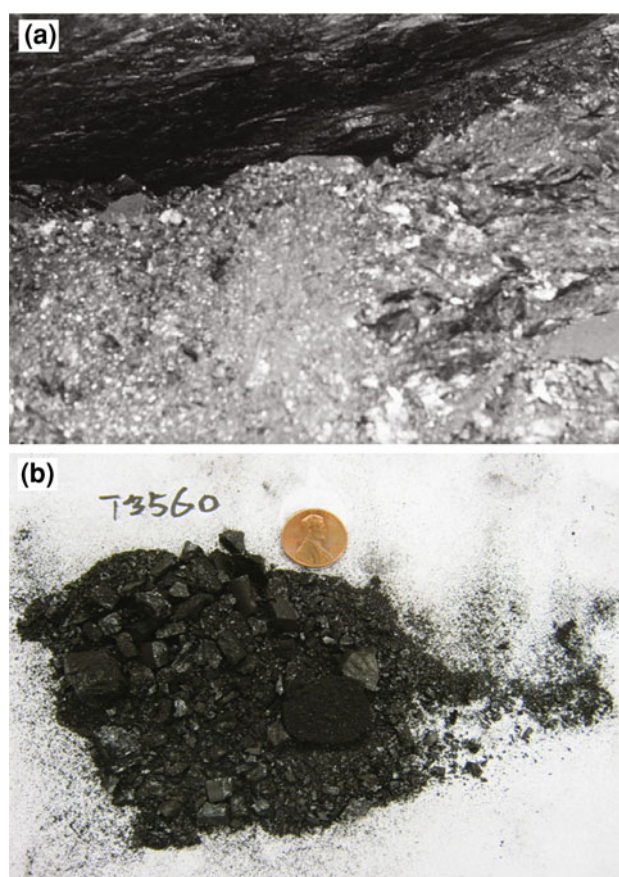


**Fig. 12** **a** In situ coal and gas outbursts induced by underground mining (Xu et al. 2006), **b** laboratory dynamically failed coal specimen in this study

(horizontal stress). Experiments on deviatoric cyclic stressing with increasing amplitude have shown that whether coal begins cracking depends primarily on the deviatoric stress level, not on the numbers of loading cycles (Wang et al. 2012b). This indicates that the underground mining-induced stress, which is dependent on coal seam properties and geometry, is an important factor in controlling the failure of coal seams.

The loading rate dependence of elastic modulus (Heerden 1985) and peak strength (Okubo et al. 2006) of coal has been studied, but no clear conclusion has been drawn in these studies due to broad scatter of the data—which is part of the innate nature of coal. However, our studies have shown some systematic effects of loading rate, especially on failure behavior, as we find that a higher loading rate produces more ductile and strain hardening failure. We also find that during loading, the maximum pore pressure increment increases with loading rate (Fig. 10a). Since the flow paths are along the direction of deviatoric loading in this study, we also observe pore pressure enhancement. But for underground coal seams, this vertical loading induced overpressure in the fractures cannot drain horizontally into

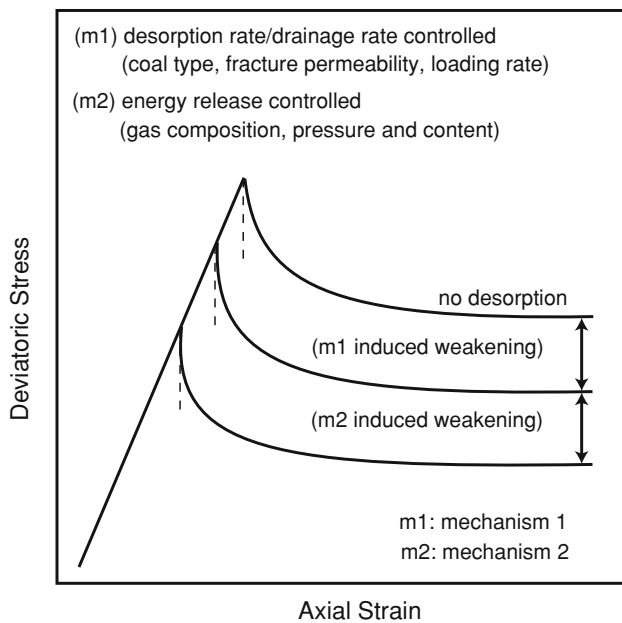


**Fig. 13** A conceptual model demonstrating the role of gas desorption on the mechanical behavior of coal through two mechanisms: (1) the effective stress effects (*m1*), controlled by the ratio of desorption rate and drainage rate, and (2) accelerating the micro-fracturing of coal due to the sudden gas expansion of the desorbed compressible gas phase (*m2*), controlled by gas composition, pressure and content. These two effects reduce both the peak and the residual strengths

the mine opening due to the inhibited drainage. Thus, the larger the loading rate the larger the overpressure in the fractures. We posit that energy release rate correlates positively with loading rate in the energetic failure of coal.

In situ gas composition is predominantly methane, carbon dioxide or a mixture of the two in underground coal and gas outbursts (Beamish and Crosdale 1998). Carbon dioxide outbursts tend to be more violent, mainly due to its larger sorption capacity. This corresponds to the results in our study because the specimen infiltrated with He exhibits a significantly larger strength. We believe that this difference is directly related to the sorption/desorption processes.

#### 4.3 Weakening Mechanisms

The effect of sorption on the mechanical strength and structure of coal has also been previously investigated. Weakening due to CO<sub>2</sub> sorption in coal is found in uniaxial (Ranjith et al. 2010; Viète and Ranjith 2006) and triaxial compression (Wang et al. 2011). Wang et al. (2011) show that the sorption of CH<sub>4</sub> and CO<sub>2</sub> has a weakening effect. The coal specimen exposed to gas in its interior for a longer time has a smaller strength than the specimen exposed to gas for a shorter time. The post-failure average particle size is smaller for the specimen exposed to gas for a longer time. This weakening effect due to gas sorption process also contributes to the overall weakening mechanisms.

Our results in this study suggest that gas desorption has two weakening effects. The first through increasing pore pressure in fractures and therefore reducing effective stress (see Fig. 9a), and the second through crushing the coal matrix in the process of desorption and facilitating rapid energy release carried by the gas phase (see Fig. 7b). It is also worth noting that small amounts of gas can help drive the violence of a coal bump. Gas may play a larger role than formerly thought in coal bumps as opposed to gas outbursts.

Figure 13 illustrates the net influence of these two weakening mechanisms due to gas desorption. The degree of weakening in the mechanical response for the first mechanism (reducing the effective stress) depends on the ratio of the gas desorption rate relative to the drainage rate from the fractures (permeability). Where the gas desorption rate is greater than the rate of gas pressure dissipation, the process will potentially run-away to failure: the larger this ratio, the more energetic the failure. Where the reverse is true, the pressure buildup feedback is negative, and the hazard of catastrophic gas-driven collapse may be largely mitigated. The effect of weakening of the mechanical properties of the coal for the second mechanism depends on the gas composition, pressure and content, as these determine the amount of energy that can be released from desorption. Strong sorptive characteristics, high gas pressure and content comprise the most favorable conditions for producing an energetic failure in coal seams.

#### 5 Conclusions

This study presents laboratory experiments designed to investigate the influence of gas desorption, stress level and loading rate on the mechanical response of methane infiltrated coal. Our results show that gas desorption weakens coal through two mechanisms: (1) reducing the effective stress controlled by the ratio of gas desorption rate over the drainage rate, and (2) crushing coal due to the internal gas energy release controlled by gas composition, pressure and content. Our results have implications for the stability of underground coal seams where gas desorption may be triggered by the mining-induced changes in the state of stress. We find that the elastic modulus and strength of coal reduces with decreasing effective confining stress, and increasing loading rate and these conditions for an underground coal seam increase the possibility that failure will be energetic.

**Acknowledgments** This work is a partial result of funding by NIOSH under contract 200-2008-25702, and the National Science Foundation under Grant EAR- 0842134. This support is gratefully acknowledged. We thank Co-Editor Herbert Einstein and two anonymous reviewers for valuable suggestions that helped improve the manuscript.

## References

- Ates Y, Barron K (1988) The effect of gas sorption on the strength of coal. *Mining Sci Technol* 6:291–300
- Aziz NI, Ming-Li W (1999) The effect of sorbed gas on the strength of coal - an experimental study. *Geotech Geol Eng* 17:387–402
- Bai M, Elsworth D (2000) Coupled processes in subsurface deformation. ASCE Press, Flow and Transport, p 336
- Beamish BB, Crosdale PJ (1998) Instantaneous outbursts in underground coal mines: an overview and association with coal type. *Int J Coal Geol* 35:27–55
- Brace WF, Paulding BW Jr, Scholz C (1966) Dilatancy in the fracture of crystalline rocks. *J Geophys Res* 71(16):3939–3953
- Brace WF, Walsh JB, Frangos WT (1968) Permeability of granite under high pressure. *J Geophys Res* 73:2225–2236
- Cao Y, He D, Glick DC (2001) Coal and gas outbursts in footwalls of reverse faults. *Int J Coal Geol* 48:47–63
- Cook NGW (1976) Seismicity associated with mining. *Eng Geol* 10:99–122
- Cyrl T (1992) A concept of prediction of rock and gas outbursts. *Geotech Geol Eng* 10:1–17
- Diaz Aguado MB, Gonzalez C (2009) Influence of the stress state in a coal bump-prone deep coalbed: a case study. *Int J Rock Mech Min Sci* 46:333–345
- Diaz Aguado MB, Gonzalez Nicieza C (2007) Control and prevention of gas outbursts in coal mines, Riosa-Olloniego coalfield, Spain. *Int J Coal Geol* 69:253–266
- Durucan S, Edwards JS (1986) The effects of stress and fracturing on permeability of coal. *Min Sci Technol* 3:205–216
- Elsworth D, Bai M (1992) Flow-deformation response of dual-porosity media. *J Geotech Eng* 118:107–124
- Faiz M, Saghaifi A, Sherwood N, Wang I (2007) The influence of petrological properties and burial history on coal seam methane reservoir characterization, Sydney Basin, Australia. *Int J Coal Geol* 70:193–208
- Gray I (1987) Reservoir engineering in coal seams: part 1-the physical process of gas storage and movement in coal seams. *SPE Reserv Eng* 2(1):28–34
- Guan P, Wang H, Zhang Y (2009) Mechanism of instantaneous coal outbursts. *Geology* 37:915–918
- Hargraves AJ (1980) A review of instantaneous outburst data. *Proc. The Occurrence, Prediction and Control of Outbursts in Coal Mines*. The Aust. Inst. Min. Metall., Melbourne, 1–18
- Harpalani S (1985) Gas flow through stressed coal, PhD thesis. University of California, Berkeley, pp 158
- Heerden WL (1985) In situ determination of the dynamic moduli of elasticity of coal. *Int J Rock Mech Min Sci Geomech Abstr* 22:339–343
- Hobbs DW (1964) The Strength and the stress-strain characteristics of coal in triaxial compression. *J Geol* 72:214–231
- Hol S, Peach CJ, Spiers CJ (2011) Applied stress reduces the CO<sub>2</sub> sorption capacity of coal. *Int J Coal Geol* 85:128–142
- Hol S, Peach CJ, Spiers CJ (2012a) Effect of 3-D stress state on adsorption of CO<sub>2</sub> by coal. *Int J Coal Geol* 93:1–15
- Hol S, Spiers CJ, Peach CJ (2012b) Microfracturing of coal due to interaction with CO<sub>2</sub> under unconfined conditions. *Fuel* 97:569–584
- Hsieh PA, Tracy JV, Neuzil CE, Bredehoeft JD, Silliman SE (1981) A transient laboratory method for determining the hydraulic properties of 'tight' rocks—Theory. *Int J Rock Mech Min Sci Geomech Abstr* 18:245–252
- Jaeger JC, Cook NGW, Zimmerman RW (2007) Fundamentals of rock mechanics, 4th edn. Wiley-Blackwell, Oxford
- Karacan CÖ, Ruiz FA, Cotè M, Phipps S (2011) Coal mine methane: a review of capture and utilization practices with benefits to mining safety and to greenhouse gas reduction. *Int J Coal Geol* 86:121–156
- Lama RD, Bodziony J (1998) Management of outburst in underground coal mines. *Int J Coal Geol* 35:83–115
- Li H (2001) Major and minor structural features of a bedding shear zone along a coal seam and related gas outburst, Pingdingshan coalfield, northern China. *Int J Coal Geol* 47:101–113
- Li X-Z, Hua A-Z (2006) Prediction and prevention of sandstone-gas outbursts in coal mines. *Int J Rock Mech Min Sci* 43:2–18
- Li T, Cai MF, Cai M (2007) A review of mining-induced seismicity in China. *Int J Rock Mech Min Sci* 44:1149–1171
- Liu MJ, Mitri HS, Wei JP (2008) Recent trends of coal and gas outburst accidents in China. In: Proceedings of the 27th International Conference on Ground Control in Mining, WV University, West Virginia, 29–31 July, pp 66–71
- Medhurst TP, Brown ET (1998) A study of the mechanical behavior of coal for pillar design. *Int J Rock Mech Min Sci* 35:1087–1105
- Okubo S, Fukui K, Qingxin Q (2006) Uniaxial compression and tension tests of anthracite and loading rate dependence of peak strength. *Int J Coal Geol* 68:196–204
- Ranjith PG, Jasinge D, Choi SK, Mehic M, Shannon B (2010) The effect of CO<sub>2</sub> saturation on mechanical properties of Australian black coal using acoustic emission. *Fuel* 89:2110–2117
- Rudnicki JW (1984) Effects of dilatant hardening on the development of concentrated shear deformation in fissured rock masses. *J Geophys Res* 89:9259–9270
- Saghaifi A, Faiz M, Roberts D (2007) CO<sub>2</sub> storage and gas diffusivity properties of coals from Sydney Basin, Australia. *Int J Coal Geol* 70:240–254
- Samuelson J, Elsworth D, Marone C (2009) Shear-induced dilatancy of fluid-saturated faults: Experiment and theory. *J Geophys Res* 114(B12):B12404
- Shepherd J, Rixon LK, Griffiths L (1981) Outbursts and geological structures in coal mines: a review. *Int J Rock Mech Min Sci Geomech Abstr* 18:267–283
- St. George JD, Barakat MA (2001) The change in effective stress associated with shrinkage from gas desorption in coal. *Int J Coal Geol* 45:105–113
- Szwedzicki T (2003) Rock mass behaviour prior to failure. *Int J Rock Mech Min Sci* 40:573–584
- Tang CA, Tham LG, Lee PKK, Yang TH, Li LC (2002) Coupled analysis of flow, stress and damage (FSD) in rock failure. *Int J Rock Mech Min Sci* 39:477–489
- Viete DR, Ranjith PG (2006) The effect of CO<sub>2</sub> on the geomechanical and permeability behaviour of brown coal: implications for coal seam CO<sub>2</sub> sequestration. *Int J Coal Geol* 66:204–216
- Wang S, Elsworth D, Liu J (2011) Permeability evolution in fractured coal: the roles of fracture geometry and water-content. *Int J Coal Geol* 87:13–25
- Wang S, Elsworth D, Liu J (2012a) A mechanistic model for permeability evolution in dual permeability dual stiffness sorbing media. *J Geophys Res* 117:B06205. doi:10.1029/2011JB008855
- Wang S, Elsworth D, Liu J (2012b) Permeability evolution during progressive deformation of intact coal: implications for instability in underground coal seams. *Int J Rock Mech Min Sci*. doi:10.1016/j.ijrmms.2012.09.005
- Wold MB, Connell LD, Choi SK (2008) The role of spatial variability in coal seam parameters on gas outburst behaviour during coal mining. *Int J Coal Geol* 75:1–14
- Xu T, Tang CA, Yang TH, Zhu WC, Liu J (2006) Numerical investigation of coal and gas outbursts in underground collieries. *Int J Rock Mech Min Sci* 43:905–919
- Zhu WC, Liu J, Sheng JC, Elsworth D (2007) Analysis of coupled gas flow and deformation process with desorption and Klinkenberg effects in coal seams. *Int J Rock Mech Min Sci* 44:971–980